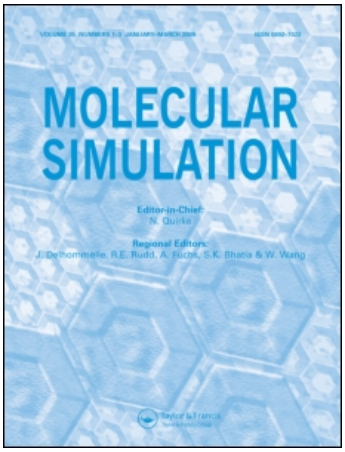

Molecular Simulation
Publication details, including instructions for authors and subscription information:
http://www.informaworld.com/smpp/title~content=t713644482

Modified single sweep method for reconstructing free-energy landscapes

M. Monteferrante[a]; S. Bonella[a]; S. Meloni[b]; G. Ciccotti[a]
[a] Department of Physics, Università di Roma 'La Sapienza', Rome, Italy [b] Consorzio per le Applicazioni del Supercalcolo per Università e Ricerca, Rome, Italy

To cite this Article Monteferrante, M. , Bonella, S. , Meloni, S. and Ciccotti, G.(2009) 'Modified single sweep method for reconstructing free-energy landscapes', Molecular Simulation, 35: 12, 1116 — 1129
To link to this Article: DOI: 10.1080/08927020903051598
URL: http://dx.doi.org/10.1080/08927020903051598

Molecular Simulation
Vol. 35, Nos. 12–13, October–November 2009, 1116–1129

Taylor & Francis
Taylor & Francis Group

Modified single sweep method for reconstructing free-energy landscapes

M. Monteferrante[a], S. Bonella[a]*, S. Meloni[b] and G. Ciccotti[a]

[a]*Department of Physics, Università di Roma 'La Sapienza', P. le A. Moro 2, 00185 Rome, Italy;* [b]*Consorzio per le Applicazioni del Supercalcolo per Università e Ricerca, CASPUR, via dei Tizii 6, 00185 Rome, Italy*

(*Received 16 March 2009; final version received 12 May 2009*)

Two modifications of the recently developed *single sweep* method to efficiently reconstruct free-energy landscapes in several dimensions are proposed. In single sweep, the free energy is estimated as a linear combination of radial basis functions whose parameters are optimised by minimising an appropriate objective function. In this work, the single variance Gaussian radial basis usually employed in single sweep when non-periodic collective variables are used is generalised to a basis of multivariate Gaussians whose covariance matrix can change with the location of the basis function on the landscape. A new objective function, aimed at a more accurate reconstruction of the landscape in the vicinity of stationary points, is also introduced. The performance of the modified single sweep is compared to that of the standard method in the reconstruction of a model benchmark potential and of the free-energy profile of a physically relevant example. The results of these comparisons show that employing the new objective function can result in an improvement of the efficiency and accuracy of the reconstruction.

Keywords: free-energy reconstruction; single sweep method; radial basis reconstruction; TAMD; activated processes; sodium alanates

1. Introduction

Activated processes as diverse as chemical reactions, conformational changes in proteins and proton transfer in intra-membrane channels can be described, in a suitable set of collective variables, as transitions between metastable states in the free energy of the system. To define this quantity, consider a system with N degrees of freedom whose coordinates are identified by the vector $\mathbf{x} = (x_1, \ldots, x_N)$. If we indicate with $\theta(x) = (\theta^1(x), \ldots, \theta^\nu(x))$ the set of ν collective variables that characterise the activated process (these can be distances, angles, coordination numbers, etc.), the corresponding free energy is

$$F(z) = -\beta^{-1} \ln Z^{-1} \int_\Omega \mathrm{e}^{-\beta V(x)} \prod_{\alpha=1}^{\nu} \delta(\theta^\alpha(x) - z^\alpha)\, \mathrm{d}x, \quad (1)$$

where $z = (z^1, \ldots, z^\nu)$ are specific realisations of the collective variables, Z is the partition function and Ω is the volume accessible to the system, $V(x)$ is the potential energy and $\beta = 1/k_\mathrm{B}T$, if T is the temperature (k_B is Boltzmann's constant). The definition above is equivalent to assigning a probability density equal to $\mathrm{e}^{-\beta F(z)}$ to the state $\theta(x) = z$ of the system. A direct calculation of this probability, based on binning the space of the collective variables and building a histogram of the frequency of their values along a dynamical trajectory, is however not a viable method for obtaining the free energy; in the presence of significant barriers, the trajectory will not explore all the relevant configurations of the system in the time scales accessible by simulation. Furthermore, the number of bins in a brute force calculation on a regularly spaced grid grows exponentially with the number of collective variables. Several methods have been proposed to perform the calculation in a more efficient way. The weighted histogram approach [1–3], thermodynamic integration [4] and, more recently, metadynamics [5,6] are some examples. In the following, we focus on the single sweep method recently proposed by Maragliano and Vanden-Eijnden [7] with the intent to explore possible generalisations of the approach. Single sweep combines two steps. The first employs the temperature-accelerated molecular dynamics (TAMD) introduced by the same authors [8] (see also [9–12] for related work) to generate a trajectory of the collective variables that efficiently explores relevant regions of the free-energy landscape even in the presence of barriers. In the second step, points along this trajectory are chosen as centres for an interpolation grid and the free energy is represented as a linear combination of radial basis functions [13,14], e.g. Gaussians centred on the grid. The use of radial basis functions improves the scaling of the method with the number of collective variables with respect to the use of a regular grid for the histogram. Both the coefficients of the linear combination and the parameters in the radial basis

*Corresponding author. Email: sara.bonella@roma1.infn.it

ISSN 0892-7022 print/ISSN 1029-0435 online

DOI: 10.1080/08927020903051598
http://www.informaworld.com

functions, a single variance for all elements in the case of Gaussian basis functions, are optimised by least square fitting of a given objective function. Single sweep has been tested in a set of increasingly challenging applications and it has been proved to accurately reconstruct complex free-energy landscapes in up to four-dimensions [7]. In this paper, we explore the possibility to further improve its efficiency by introducing two variations in the procedure. First, focusing on the choice of Gaussian radial basis functions, we investigate the effect of substituting the single variance of the standard procedure with a covariance matrix that can change at the different centres. Second, we propose a simple modification to the objective function that aims at a more accurate reconstruction of the free energy in the proximity of stationary points. As these often define the regions of the landscape – minima and saddle points – that are more interesting to characterise an activated process, this increased accuracy might prove important in applications. The paper is organised as follows.

The theory section begins with a summary of the single sweep method. A detailed derivation of the method can be found in reference [7]; here we highlight its most relevant features for convenience. The second part of the theory section describes the generalisations we propose. An algorithm to optimise the parameters in the interpolated free energy is presented in the appendix. In the results section we compare the performance of the modified single sweep method with that of the original scheme by first considering a standard benchmark model calculation, the reconstruction of the Müller potential [15] and then by revisiting a physical example, the reconstruction of the free energy associated to an activated diffusion process in sodium alanate [16]. Conclusions end the paper.

2. Theory

2.1 Single sweep summary

Single sweep combines two complementary steps: efficient exploration of the free-energy landscape via a TAMD trajectory and global reconstruction of the free energy as a linear combination of optimised radial basis functions centred at appropriate points along the trajectory. The modifications of the standard method that we intend to test involve only the second part of the procedure, and we shall focus on those in Section 2.2. For completeness, however, we begin by summarising the main features of the standard method.

2.1.1 Temperature-accelerated molecular dynamics

In TAMD, new dynamical variables $z = (z^1, \ldots, z^\nu)$ are introduced alongside the physical degrees of freedom, and an extended Lagrangian for the system is defined by setting up the kinetic energy term of the z variables and modifying the original potential energy term. The new total potential contains, in addition to the physical potential energy $V(x)$, a quadratic term that couples the collective variables $\theta(x)$ to the new variables z, thus

$$U_\kappa(x,z) = V(x) + \frac{\kappa}{2}\sum_{\alpha=1}^{\nu}(\theta^\alpha(x) - z^\alpha)^2 \tag{2}$$

where κ is a constant whose dimensions depend on the nature of the collective variables. It is further assumed that the z variables, to which a fictitious mass $\bar{m}$ can be assigned, evolve at a fictitious temperature $\bar{T}$ different from that of the physical system. In the following, we shall outline the method using Langevin dynamics for the time evolution, but any dynamics that generates the canonical distribution can be used [12]. If we assign friction coefficients γ and $\bar{\gamma}$ to the physical degrees of freedom and to the z variables, respectively, the evolution of the extended system is governed by the following set of coupled equations

$$\begin{aligned} m\ddot{x} &= -\nabla_x V(x) - \kappa\sum_{\alpha=1}^{\nu}(\theta^\alpha(x) - z^\alpha)\nabla_x\theta^\alpha(x) - \gamma\dot{x} \\ &\quad + \sqrt{2\beta^{-1}\gamma}\eta^x, \\ \bar{m}\ddot{z} &= \kappa(\theta(x) - z) - \bar{\gamma}\dot{z} + \sqrt{2\bar{\beta}^{-1}\bar{\gamma}}\eta^z, \end{aligned} \tag{3}$$

where $\bar{\beta} = 1/k_B\bar{T}$, and η^x and η^z are the white noise associated with the Langevin evolution of the physical and new variables. Adiabatic separation of the motion of the physical and fictitious variables can be induced by increasing the value of $\bar{m}(\gg m)$ and $\bar{\gamma}(\gg\gamma)$, with the condition that $\bar{m} = O(\bar{\gamma}^2)$. In these conditions, the z variables evolve, on the slower time scale of their motion, according to an effective force which is obtained by averaging the right-hand side of the second equation in system (3) with respect to the distribution that thermalises the fast, physical variables. This distribution is the conditional probability density function for the evolution equation of the physical variables at $z(t) = z$ fixed. The conditional probability density is given by $\rho(x|z) = Z_\kappa^{-1}(z)\,\mathrm{e}^{-\beta U_\kappa(x,z)}$ with $Z_\kappa(z) = \int \mathrm{d}x\,\mathrm{e}^{-\beta U_\kappa(x,z)}$. The only term affected by the average in the evolution equation for the z variables is the one proportional to κ and the effective evolution equation obtained after performing this average can be written as

$$\bar{m}\ddot{z} = -\nabla_z F_\kappa(z) - \bar{\gamma}\dot{z} + \sqrt{2\bar{\beta}^{-1}\bar{\gamma}}\eta^z, \tag{4}$$

where we have defined

$$F_\kappa(z) = -\beta^{-1} \ln \mathcal{Z}_\kappa^{-1} \int \mathrm{d}x \, \mathrm{e}^{-\beta U_\kappa(x,z)},$$

$$= -\beta^{-1} \ln \mathcal{Z}_\kappa^{-1} \int \mathrm{d}x \, \mathrm{e}^{-\beta V(x)} \, \mathrm{e}^{-(\beta\kappa/2)\sum_{\alpha=1}^{\nu}(\theta^\alpha(x) - z^\alpha)^2} \quad (5)$$

with $\mathcal{Z}_\kappa = \int \mathrm{d}x \, \mathrm{d}z \, \mathrm{e}^{-\beta U_\kappa(x,z)}$, so that

$$-\nabla_z F_\kappa(z) = Z_\kappa^{-1}(z) \int \mathrm{d}x \, \kappa(z - \theta(x)) \mathrm{e}^{-\beta U_\kappa(x,z)}. \quad (6)$$

In the limit $\beta\kappa \to \infty$, the Gaussian function in Equation (5) tends to a delta function in the argument $(\theta^\alpha(x) - z^\alpha)$ and $F_\kappa(z)$ becomes the free energy of the *physical* system at inverse temperature β. Remarkably then, in the appropriate limits for the parameters in the extended Lagrangian, the fictitious variables evolve based on the free-energy landscape at the physical temperature and their trajectory can thus be used to explore this landscape. Moreover, the evolution equation holds for any value of $\bar{T}$. This quantity can be increased to a point where the thermal energy of the fictitious variables is high enough to overcome the physical system's free-energy barriers and the z trajectory can visit the relevant metastable and transition regions at least once in a reasonable amount of time. This feature makes points along the TAMD trajectory ideal centres for elements of the radial basis set to be used for the global reconstruction of the free energy. In a single sweep calculation, centres are deposed along the trajectory based on a distance criterion: beginning with the value $z_1 = z(0)$ a new point is added to the set when its distance from all other members of the set exceeds a given threshold d. For a fixed trajectory length, the parameter d controls the size of the set of centres and it is adjusted to reach convergence of the free-energy reconstruction with the number of centres.

2.1.2 *Radial basis reconstruction*

Given the set of centres $\{z_1, \ldots, z_K\}$ in the space of the ν collective variables, single sweep estimates the free energy as a linear combination of radial basis functions, thus

$$\tilde{F}(z) = \sum_{k=1}^{K} a_k \phi_\sigma(|z - z_k|). \quad (7)$$

In the following, we shall consider the case $\phi_\sigma(r) = \mathrm{e}^{-r^2/2\sigma^2}$, but other radial basis functions can be used. The coefficients a_k and the width σ (a positive number common to all basis elements and to all directions) are adjusted by minimising the objective function

$$E(a, \sigma) = \sum_{k=1}^{K} \sum_{\alpha=1}^{\nu} [f_k^\alpha + \nabla_\alpha \tilde{F}(z_k)]^2. \quad (8)$$

In the definition above, f_k is the negative gradient of the free energy, i.e. $f_k = -\nabla F(z_k)$. This quantity, also known as the mean force, can be estimated as a local conditional average via Equation (6) and, a part from the location of the centres, is the only input needed in the reconstruction procedure. Once the mean forces at the centres have been computed, the coefficients and the variance in Equation (7) can be optimised as follows: for a fixed value of σ, the optimal set of coefficients is the solution, indicated as a^*, of the linear system

$$\sum_{k'=1}^{K} B_{k,k'}(\sigma) a_{k'}(\sigma) = c_k(\sigma), \quad (9)$$

where

$$B_{k,k'} = \sum_{k''=1}^{K} \nabla\phi_\sigma(|z_k - z_{k''}|) \cdot \nabla\phi_\sigma(|z_{k''} - z_{k'}|) \quad (10)$$

and

$$c_k = -\sum_{k'=1}^{K} \nabla\phi_\sigma(|z_k - z_{k'}|) \cdot f_{k'}. \quad (11)$$

The optimal σ, indicated as σ^*, satisfies $E(a^*(\sigma^*), \sigma^*) = \min_\sigma E(a^*(\sigma), \sigma)$ and can be found by a brute force computation of the residual $E(a^*(\sigma), \sigma)$ for increasing values of σ starting from the distance of the centres. While this choice of the initial value for the scan on the sigma grid is empirical, it has proved effective in all applications considered so far. This choice can be motivated by observing that the objective function involves a linear combination of the gradients of the basis function, e.g.

$$\nabla\phi_\sigma(|z_k - z|) = \frac{|z_k - z|}{\sigma^2} \phi_\sigma(|z_k - z|). \quad (12)$$

In the objective function then, the basis element centred at z_k does not contribute to estimating the mean force computed at z_k and this mean force must be reconstructed via the basis elements centred at the neighbouring points. This is possible only if the variance of the basis functions is such that they have a finite value at z_k. The prescription on the minimum value of σ is a sufficient, though not necessary, condition for meeting this criterion.

It is known that the stability of the system of equations which determines the coefficients in the radial-basis representation can deteriorate quite dramatically with the number of centres [14]. To control numerical instabilities

in the solution, the condition number of the matrix **B** is monitored [17]. This quantity is defined as

$$\kappa(\mathbf{B}) = \mu_K(\mathbf{B})/\mu_1(\mathbf{B}), \tag{13}$$

where $\mu_k(\mathbf{B})$ is the kth singular value of **B** in order of increasing magnitude (the singular values of the matrix **B** are the square root of the eigenvalues of $\mathbf{B}^T\mathbf{B}$). The maximum condition number observed in the calculations reported here was 10^8, below the threshold (10^{14}) that could cause problems for the numerical inversion of the matrix in double precision calculations. After optimisation of the parameters, the accuracy of the reconstructed free energy can be assessed using, for example, the relative residual

$$R = \sqrt{\frac{E(a^*, \sigma^*)}{\sum_{k=1}^{K} |f_k|^2}}. \tag{14}$$

2.2 Variations on the single sweep theme

2.2.1 Allowing for more than one σ

As mentioned above, in the standard version of single sweep σ is chosen to be the same for all radial-basis functions and all components of the vector **z**. In the following, we investigate the selection of different widths for different centres and/or different components of z as a tool to increase the accuracy of the method. To that end, the definition of the basis function in Equation (7) is generalised as

$$\Phi_{\Sigma_k}(|z - z_k|) = \mathrm{e}^{-(1/2)(z-z_k)^{\mathrm{T}}\Sigma_k^{-1}(z-z_k)}. \tag{15}$$

The $\nu \times \nu$ positive definite matrix Σ_k^{-1} is the inverse of the covariance matrix associated with the centre z_k, defined as

$$(\Sigma_k)_{\alpha,\beta} = \sigma_{k,\alpha}\sigma_{k,\beta}(\delta_{\alpha,\beta} + \rho_{k,\alpha,\beta}), \tag{16}$$

where the correlation coefficient, symmetric with respect to the indexes α, β is such that $|\rho_{k,\alpha,\beta}| \leq 1$ if $\alpha \neq \beta$ and $\rho_{k,\alpha,\alpha} = 0$. Of course, if $\rho_{k,\alpha,\beta} = 0 \forall \alpha, \beta$ and $\sigma_{k,\alpha}^2 = \sigma^2$ for all k and α the definition above reduces to the standard, single sigma, case. We will indicate with $\{\Sigma\}$ the elements of the covariance matrix. The prescription for adjusting the coefficients, $a_k(\Sigma)$, and the matrix elements $\{\Sigma\}$ to optimise the representation of the free energy is the same as that of the standard single sweep, i.e. minimisation of an objective function. If the standard choice, Equation (8), for the objective function is preserved, this translates, for fixed Σ, into solving the linear system

$$\sum_{k'=1}^{K} \bar{B}_{k,k'}(\Sigma) a_{k'}(\Sigma) = \bar{c}_k(\Sigma), \tag{17}$$

where

$$\bar{B}_{k,k'} = \sum_{k''=1}^{K} \nabla\Phi_\Sigma(|z_k - z_{k''}|) \cdot \nabla\Phi_\Sigma(|z_{k''} - z_{k'}|), \tag{18}$$

$$\bar{c}_k = -\sum_{k'=1}^{K} \nabla\Phi_\Sigma(|z_k - z_{k'}|) \cdot f_{k'}.$$

In this case, however, the increased dimensionality of the Σ space makes a brute force minimisation of the residual with respect to the parameters $\{\sigma_{k,\alpha}, \rho_{k,\alpha,\beta}\}$ problematic and alternative techniques must be used. In this work, we used a simulated annealing scheme [18], as summarised in the appendix.

2.2.2 Modifying the objective function

Alternative choices of the objective function can easily be incorporated in the single sweep method. In this work, we introduce and test the following:

$$E_r(a, \Sigma) = \sum_{k=1}^{K} \sum_{\alpha=1}^{\nu} \epsilon_k^\alpha [f_k^\alpha + \nabla_\alpha \tilde{F}(z_k)]^2, \tag{19}$$

where $\epsilon_k^\alpha = 1/f_k^{\alpha^2}$. The function above will be indicated as 'relative objective function' and it differs from the one used in standard single sweep by the introduction of a weight equal to the inverse of the square of the mean force in each term of the sum. This weight reduces the importance on the interpolation parameters' optimisation of centres located in regions of particularly high gradient of the landscape while amplifying the relevance of (almost) stationary points of the landscape. Since the stationary points are associated with the location of basins and/or saddle points of the free energy – and thus with the regions corresponding to the initial, final and transition state of the activated event – a reconstruction procedure that is more accurate around them should characterise the process more precisely. The proposed objective function should also provide a more accurate reconstruction of the steepest descent path, i.e. the curve characterised by the condition that the orthogonal component of the mean force is zero along the path. This path is often used as an approximation to the transition path as defined in ref. [19]. If a centre is located exactly at a point such that $f_k^\alpha = 0$, the definition above becomes singular. This problem can, however, be solved via the introduction of a small additive term at the denominator. In the calculations described in Section 3, it was verified that the results are stable for changes in the values of this parameter. The optimisation of the interpolation parameters follows the usual steps. Minimisation of the new objective function with respect to the coefficients for a fixed set of $\{\Sigma\}$ values leads

to solving the linear system

$$\sum_{k'=1}^{K} \tilde{B}_{k,k'}(\Sigma) a_{k'}(\Sigma) = \tilde{c}_k(\Sigma), \tag{20}$$

where now

$$\tilde{B}_{k,k'} = \sum_{k''=1}^{K} \sum_{\alpha=1}^{\nu} \epsilon_k^{\alpha} \nabla_{\alpha} \Phi_{\Sigma_{k''}}(|z_{k''} - z_k|) \nabla_{\alpha} \Phi_{\Sigma_{k''}}(|z_{k''} - z_{k'}|)$$

$$\tilde{c}_k = -\sum_{k'=1}^{K} \sum_{\alpha=1}^{\nu} \epsilon_{k'}^{\alpha} f_{k'}^{\alpha} \nabla_{\alpha} \Phi_{\Sigma_{k'}}(|z_{k'} - z_k|). \tag{21}$$

In this case too, simulated annealing is performed to identify the optimal parameters in the covariance matrix.

3. Results I: the Müller potential

In this section, we compare the performance of the modified single sweep with that of the standard method in a test problem: the reconstruction of the Müller potential. The method described in the previous sections can be adapted to reconstructing potentials by setting $\theta^i(x) = x_i$ for all i, which implies $F(z) = V(x)$ (in these expressions, $x = (x_1, \ldots, x_N)$, $\theta(x) = (\theta^1(x), \ldots, \theta^{\nu}(x))$, and $z = (z^1, \ldots, z^{\nu})$). When reconstructing potentials, the dynamics of the system can be accelerated by acting directly on its temperature and it is not necessary to introduce the z variables. The Müller potential is defined as

$$V(x, y) = \sum_{i=1}^{4} A_i \, \mathrm{e}^{a_i(x-x_i)^2 + b_i(x-x_i)(y-y_i) + c_i(y-y_i)^2} \tag{22}$$

(with the same parameters defined in [15] and summarised in Table 1). In the following, we shall indicate the two-dimensional position vector as $\mathbf{x} \equiv (x, y)$. To obtain appropriate sets of centres $\mathbf{x}_k = (x_k, y_k)$, the potential was explored by propagating a Langevin trajectory $\mathbf{x}(t)$ with initial conditions $(x(0), y(0)) = (1.0, 0.0)$ and $(\dot{x}(0), \dot{y}(0)) = (\sqrt{k_B T/2}, \sqrt{k_B T/2})$, at a temperature $T = 45$. The mass, friction coefficient and time step were chosen as $m = 1$, $\gamma = 0.8$ and $\mathrm{d}t = 5 \times 10^{-4}$. Arbitrary units are used throughout this section. The trajectory was integrated using an algorithm accurate to order $\mathrm{d}t^{1/2}$ ($\mathrm{d}t$ is the integration time step) that can be found in [20]. In the calculations reported here, two sets of 58 and 95 centres were deposed according to the standard single sweep criterion (see end of Section 1) with deposition thresholds $d = 0.4$ and 0.3, respectively. Given the temperature and the initial conditions chosen, the trajectory explores parts of the potential with different characteristics (see Figure 1 for reference). Consider first the region $x \in [-1.5, 1.0]$, $y \in [-0.25, 2.0]$. This is the part of the Müller potential used most often in test calculations since it displays the richest structure: three minima of different depth, separated by energy barriers of different height, are located there. A second region of interest for our tests consists of the borders of the contour lines shown in the figure and of a relatively vast plateau located approximately at $x \in [-2.5, -0.75]$, $y \in [0.5, 2.25]$. These are parts of the potential that include rather disparate values of the gradients, ranging from very small values on the plateau to relatively large ones at the borders. We performed two sets of runs corresponding to the two possible choices for the objective function (standard and relative). In each set we used both the original prescription for the Gaussian's variance, i.e. a single value common to all centres (results labelled as 1Sig) and the multivariate version of the basis set, using either a diagonal or a non-diagonal form for the Σ matrix. We report results for the following cases: $(\Sigma_k)_{\alpha,\beta} = \delta_{\alpha,\beta}\, \sigma_{\alpha}^2$, i.e. the variance can vary with the direction in the collective variable space, but not with the centre (these results are labelled $1 \times$ CV); $(\Sigma_k)_{\alpha,\beta} = \delta_{\alpha,\beta} \sigma_{k,\alpha}^2$, i.e. the variance can change both with direction and centre, but the matrix remains diagonal (results labelled as 'Diag sigma'); $(\Sigma_k)_{\alpha,\beta} = \sigma_{k\alpha}\sigma_{k,\beta}(\delta_{\alpha,\beta} + \rho_{k,\alpha,\beta})$, i.e. the full covariance matrix is employed (results labelled as Full sigma). Note that, when the $1 \times$ CV calculations are performed for this model problem, it is not strictly necessary to use the simulated annealing scheme outlined in the appendix since the minimisation with respect to the σ_{α}^2 can be done by scanning their values on a two-dimensional grid. Nonetheless, we have implemented the annealing also in this case and used the grid calculation as a test of the Monte Carlo scheme, and of our code, in view of the more general Diag and Full simulations. The relative quality of the results of the different runs was assessed by comparing the quantity

$$e_1 = \frac{\int_{\Omega} \mathrm{d}\mathbf{x} |V(\mathbf{x}) - \tilde{V}(\mathbf{x})|}{\int_{\Omega} \mathrm{d}\mathbf{x} |V(\mathbf{x})|}, \tag{23}$$

Table 1. Parameters for the Müller potential.

$A_1 = -200$	$a_1 = -1$	$b_1 = 0$	$c_1 = -10$	$x_1 = 1$	$y_1 = 0$
$A_2 = -100$	$a_2 = -1$	$b_2 = 0$	$c_2 = -10$	$x_2 = 0$	$y_2 = 0.5$
$A_3 = -170$	$a_3 = -6.5$	$b_3 = 11$	$c_3 = -6.5$	$x_3 = -0.5$	$y_3 = 1.5$
$A_4 = 15$	$a_4 = 0.7$	$b_4 = 0.6$	$c_4 = 0.7$	$x_4 = -1$	$y_4 = 1$

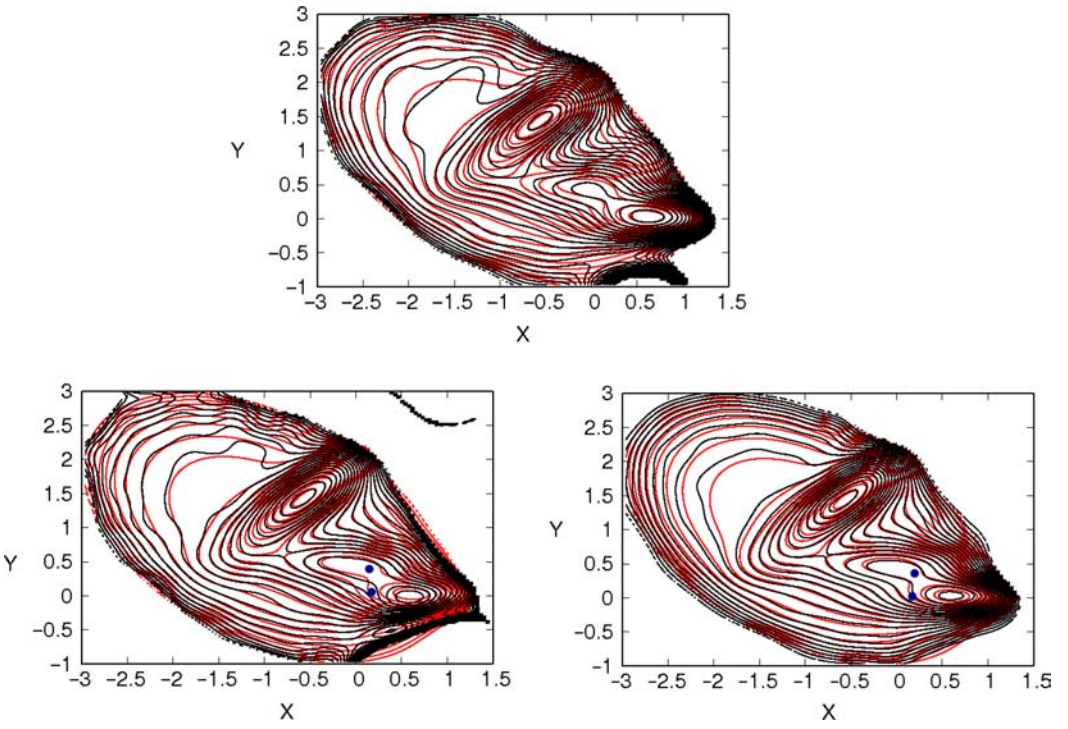

Figure 1. Müller potential: Contour lines of the potential from 0 to 290. The red curves in all panels are the exact contour lines. The potential was reconstructed deposing 95 centres ($d = 0.3$) along a Langevin trajectory with $T = 45$. Black curves in the top panel are the contour lines obtained with the standard single sweep method (1Sig); the black curves in the figure on the left in the lower panel were obtained with standard objective function, and σ varying with direction and centre (Diag sigma run); the black curves in the figure on the right in the lower panel are also for a Diag sigma run, but the relative objective function was used in the reconstruction.

where $\tilde{V}$ is the potential obtained using single sweep. e_1 was computed on a 200 × 200 grid with $x \in [-3.0, 1.5]$ and $y \in [-1.0, 3.0]$ and the integration domain Ω is specified by the condition that the original potential remains less than 290 above its minimum value. The stability of the results with respect to the simulated annealing was verified by changing the cooling protocol and by starting runs from different initial conditions for

Table 2. Müller potential: Values of the error indicators and condition number for increasing number of centres, K, and decreasing value of the deposition threshold, d. The objective function in the top table is $E(a, \Sigma)$, while the one used in the bottom table is $E_r(a, \Sigma)$. Results are reported for the standard method (1Sig), for runs in which σ can vary with direction but not with centre (1 × CV), runs in which σ can vary both with direction and centre (Diag) and runs that employ the full covariance matrix (Full).

	1Sig	1 × CV	Diag	Full
$d = 0.4$, $K = 58$				
$R \times 10^{-2}$	22.4	18.8	7.3	6.3
e_1	9.7×10^{-1}	1.1	7.8×10^{-1}	7.6×10^{-1}
$\kappa(B)$	1.2×10^{4}	5.1×10^{3}	6.8×10^{3}	6.4×10^{3}
$d = 0.3$, $K = 95$				
$R \times 10^{-2}$	14.4	8.9	4.1	3.6
e_1	4.3×10^{-1}	2.2×10^{-1}	3.8×10^{-1}	4.0×10^{-1}
$\kappa(B)$	5.8×10^{6}	1.2×10^{3}	9.0×10^{5}	1.1×10^{6}
$d = 0.4$, $K = 58$				
$E_r/K \times 10^{-2}$	5.2	4.4	3.5	0.5
e_1	7.6×10^{-1}	5.8×10^{-1}	5.1×10^{-1}	3.2×10^{-1}
$\kappa(\tilde{B})$	4.1×10^{3}	4.1×10^{3}	7.1×10^{3}	4.2×10^{3}
$d = 0.3$, $K = 95$				
$E_r/K \times 10^{-2}$	2.8	2.0	1.2	0.4
e_1	4.4×10^{-1}	4.6×10^{-1}	2.4×10^{-1}	9.5×10^{-2}
$\kappa(\tilde{B})$	1.2×10^{4}	1.8×10^{4}	9.5×10^{3}	1.8×10^{4}

$\{\sigma_{k,\alpha}, \rho_{k,\alpha,a}\}$. Table 2 summarises the results. The top panel reports the outcome of calculations for 58 and 95 centres based on the standard objective function but with increasing flexibility in the covariance matrix. As it can be seen, using the Σ matrix in any of its new forms reduces the residual R. To this reduction, however, corresponds a non-monotonous and relatively minor improvement in the accuracy of the reconstruction as measured by e_1. The situation is more regular when the relative objective function is employed (bottom part of Table 2). In this case too, a reduction of the relative error is observed as we increase the flexibility in the basis set. The correlation of this reduction with the improvement in e_1 is more pronounced than in the previous case and the values obtained for this quantity are, generally, smaller. The improvements caused by the Σ matrix and the new objective function can also be appreciated by comparing directly the original and reconstructed Müller potentials, as in Figure 1. In the figure, we superimpose the contour lines of the exact potential (red curves) on those obtained via three different single sweep reconstructions (black curves) with equal number of centres ($K = 95$). In the top panel, we plot the reconstruction based on the standard method (1Sig). In the bottom panel, we show results for the Diag sigma runs with standard (left) and relative (right) objective functions. Both modifications of the single sweep improve the reconstruction. The result obtained with the relative objective function is the most accurate, and the quality of the agreement with the exact result is essentially the same on the entire landscape, irrespective of the considerable differences in the gradients in the different regions of the potential. By increasing the number of centres, all calculations eventually converge to a very accurate reconstruction of the potential. It is, however, desirable, especially in applications in which *ab initio* molecular dynamics must be used, to understand which method behaves better with a relatively small set of $\{z_k\}$. In Figure 1, the blue dots centred at $\mathbf{x} \approx (0.225, 0.35)$ and $(0.15, 0.02)$ identify centres, where the different choice of the objective function has a particularly

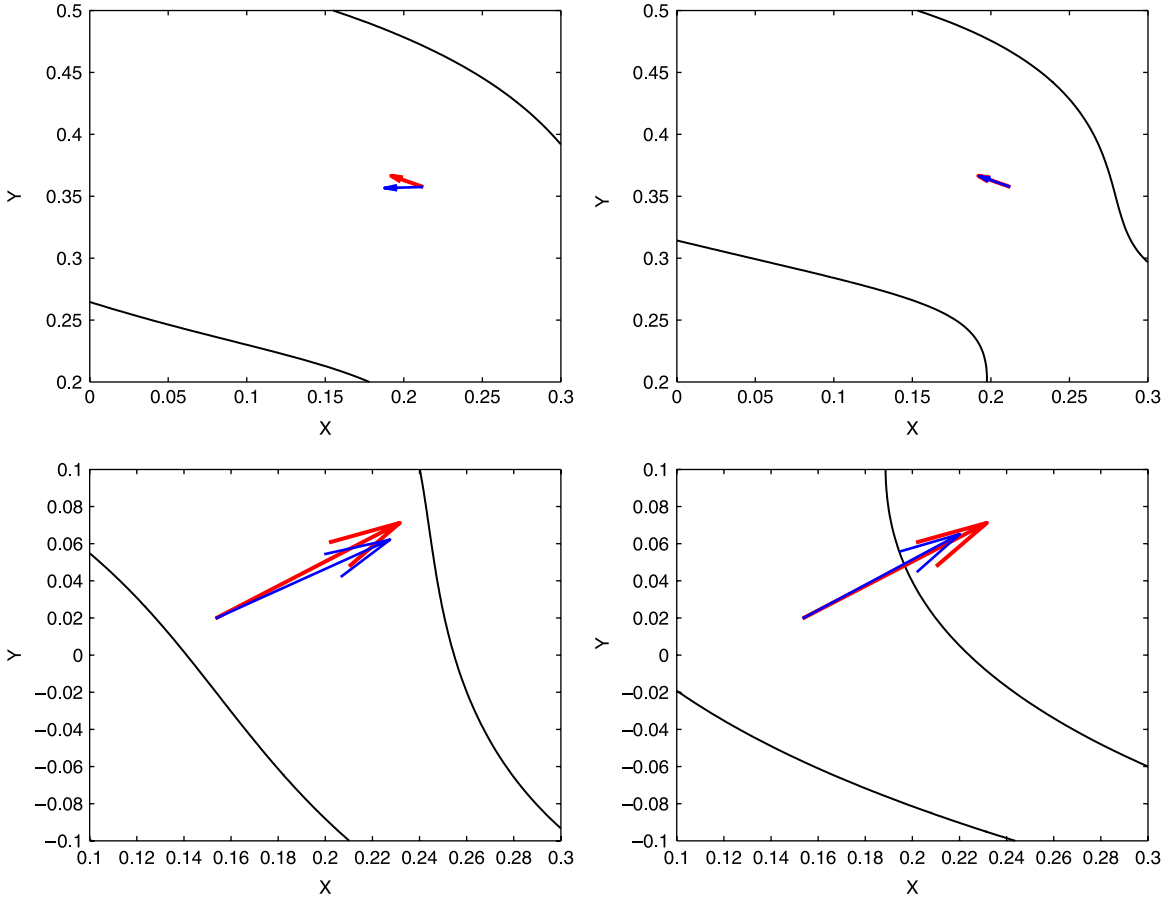

Figure 2. Müller potential: Comparison of the exact (red arrows) and reconstructed (blue arrows) gradients superimposed to the reconstructed potential (black contour lines), in a Diag sigma run at $T = 45$ in which 58 centres were deposed ($d = 0.3$). The vectors originate at the centres identified in Figure 1. The top panel shows an enhancement of the region around the centre located at $\mathbf{x} \approx (0.225, 0.35)$, the bottom panel shows an enhancement of the region around $\mathbf{x} \approx (0.15, 0.02)$. In both panels, the figure on the left shows results for the standard objective function, while results for the relative objective function are shown on the right.

noticeable effect. In Figure 2, we show enhancements of the potential around these centres. The top panel of the figure compares the exact (red arrow) and reconstructed (blue arrows) gradients for $\mathbf{x} \approx (0.225, 0.35)$ and standard (right panel) and relative (left panel) objective functions. The bottom panel compares the same quantities computed at $\mathbf{x} \approx (0.15, 0.02)$. In both cases, the values of the gradients are small as these centres lie close to the minima and using the relative objective function improves the accuracy of the reconstructed forces. This improvement is reflected in the more accurate reconstruction of the contour lines around the double minimum in Figure 1. The better performance of the relative objective function in reconstructing gradients of smaller modulus is verified essentially at all centres. In Figure 3, we show further evidence of this on a subset of relevant centres (we avoid showing the complete series for clarity of the figure). In the figure, the x-axis is labelled with the index of each centre. The continuous line connects the absolute value of the exact force, $|f_k| = |-\nabla_{\mathbf{x}} V(\mathbf{x}_k)|$, calculated at centre k. The blue error bars measure the difference between the exact forces and those computed as the gradient of the potential $\tilde{V}(\mathbf{x})$ reconstructed using the Diag sigma single sweep with the standard objective function. This difference is computed as

$$\delta f_k = \left| f_k + \sum_{k'=1}^{K} a_{k'} \nabla_{\mathbf{x}} \phi_{\Sigma}(|\mathbf{x}_k - \mathbf{x}_{k'}|) \right|. \qquad (24)$$

The red error bars represent the same quantity calculated for the Diag sigma single sweep run that employs the relative objective function. For $|f_k| > 300$, the gradient of the potential reconstructed using the standard objective function is more accurate. For $|f_k| < 100$ the situation changes, and it is the relative objective function that provides, again with very few exceptions, the more accurate representation of the true gradient.

3.1 *Scaled Müller potential*

Since in the generalised single sweep the parameters in the radial basis can change depending on the location of the centres, the shape of the Gaussian functions can vary with the local characteristics of the landscape. This effect can indeed be seen in Figure 4, where we superimpose the ellipses obtained using, as semi-axis, the values of the variances along the different directions and at the different centres on the contour lines of the exact potential for two of the runs performed in the previous subsection. The top panel shows the ellipses for the Diag sigma single sweep calculation with the standard objective function and the bottom panel shows those for the Diag sigma single sweep calculation with the relative objective function. The axes of the ellipses have been scaled by a factor of three to make the figures more intelligible. Considerable variations of the shape of the ellipses are observed, in particular for the relative objective function, but establishing a clear correlation of these variations with the properties of the landscape at the different centres is not easy. This is a consequence of the fact that the reconstruction proceeds by minimising a global objective function so that the characteristics of the basis function at a given point are determined by the gradients of the potential at all other centres and not just by the local properties of the landscape. A clearer relationship among the characteristics of the ellipses and those of the landscape can, however, be obtained for potentials that show a relevant anisotropy. As an illustrative example, we present results obtained for

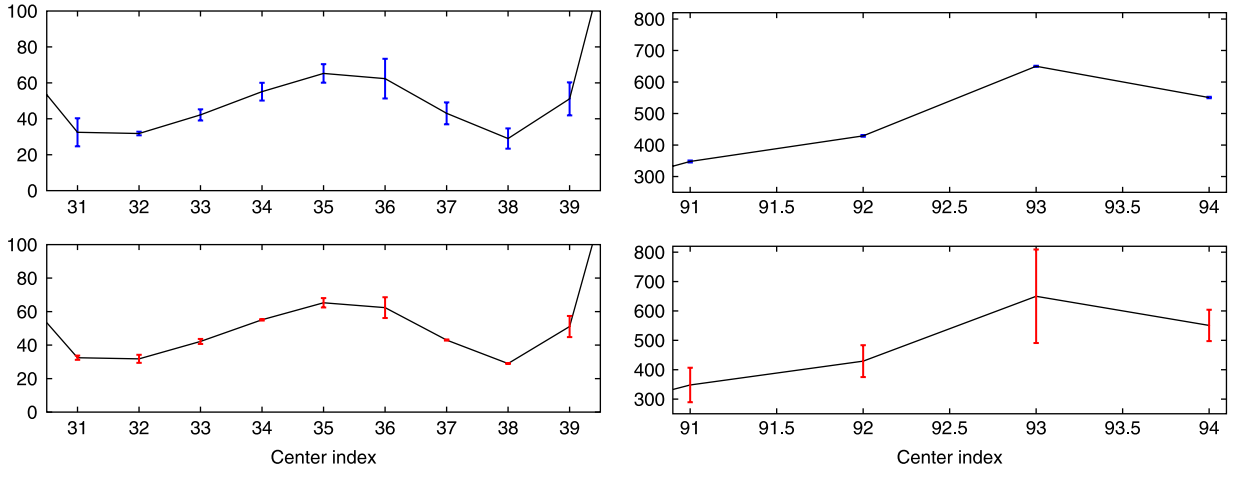

Figure 3. Error bars associated with the reconstructed mean force at the centres. The objective function is $E(a, \sigma)$ for the blue error bars and $E_r(a, \sigma)$ for the red ones. $T = 45$, $d = 0.3$ and multi-sigma runs. The line connects points representing the value of the modulus of the force at different centres. The x-axis is labelled by the centre index.

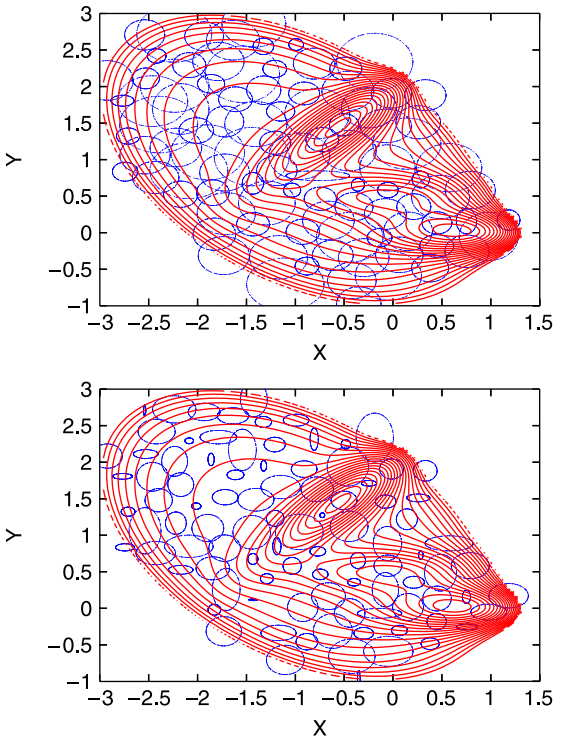

Figure 4. Ellipses with axes given by the $\sigma_{k,\alpha}$ at the centres (blue curves) superimposed on the exact contour lines of the Müller potential. The objective function is $E(a,\sigma)$ in the top panel and $E_r(a,\sigma)$ in the bottom panel. $T = 45$, $d = 0.3$ and Diag sigma runs.

a modified version of the Müller potential in which the y variable is scaled by a parameter λ, thus

$$V_\lambda(x,y) = V(x,\lambda y) \tag{25}$$

(see Equation (22) for the definition of V). In this case, we restrict our attention to the region corresponding to the basins of the three main minima. This region can be explored using a temperature lower than that used in the previous calculations, so we set $\beta = 1/26$ in the Langevin trajectory. All other parameters in the run are unchanged. We performed three sets of calculations with $\lambda = 1, 2, 3$. As in the previous case, for each value of the scaling parameter, we compared the performance of the original (1Sig) single sweep with that of different 1 × CV, Diag and Full calculations in which the standard and the relative objective functions were used. The results at the top of Table 3 are for $\lambda = 1$ (standard Müller potential) and $K = 38$ for the standard (upper part of the table) and relative (bottom part of the table) objective functions. The trends observed in these calculations are comparable to those obtained in the previous section. Note that the advantage of using the relative objective function rather than the standard one is less pronounced than in the calculation with $T = 45$. This is due to the fact that the region of the potential explored at $T = 26$ shows a more homogeneous set of gradients, so that the presence of the weight in the relative objective function is not as relevant. The last line in the two panels of the top table shows the values of the variances obtained for the standard and the 1 × CV calculations. Both in the top and bottom panel, the optimised values in the 1 × CV results remain quite close to the optimal single sigma value, but they show a slight asymmetry with $\sigma_x > \sigma_y$. As the scaling parameter is increased to $\lambda = 2$ and 3, see middle and bottom parts of Table 3, respectively, the advantage of the additional flexibility in the Σ matrix becomes more apparent and the correlation among the value of the objective function (R or E_r) and the improvement of the error estimator e_1 is more pronounced. In the case of the 1 × CV calculations, the asymmetry among σ_x and σ_y is also accentuated as the Gaussian basis functions adapt to the anisotropy of the potential induced by the scaling. The trends of the potentials reconstructed with the different variations of the single sweep method are similar; here we show results for just one characteristic situation. Figure 5 compares the reconstructed potentials (black curves) with the exact one for the case $\lambda = 3$ for the standard method (top panel) and 1 × CV calculations with the standard (bottom panel, figure on the right) and relative (bottom panel, figure on the left) objective functions. The distortion of the contour lines for the standard single sweep is quite apparent and it affects, in particular, the reconstruction of the basin of the double minimum. The 1 × CV calculation with the standard objective function agrees better with the exact results, in particular around the double minimum, but it is still affected by some distortion at the edges. The run with the relative objective function, on the other hand, provides an accurate picture of the potential in the entire range of values of (x, y) considered. The characteristics of the reconstructed forces are very similar to those reported in the previous section: for all values of λ, using the relative objective function results in a more precise calculation of smaller gradients.

4. Results II: non-local hydrogen diffusion in sodium alanates

To test the proposed modifications to single sweep in a more realistic application, we revisit a recent calculation on sodium alanates, compounds relevant in the search for technologically viable materials for solid-state hydrogen storage [21]. A detailed description of the problem addressed in the calculation, of the model adopted for the alanates, and of the simulation performed can be found in [16]. In that work, we combined standard single sweep with *ab initio* molecular dynamics (MD) of an Na_3AlH_6 crystal to discriminate among different chemical species diffusing in the system in the presence of an H vacancy. This was done by reconstructing the free-energy

Table 3. Scaled Müller potential: Deposition threshold, d, number of centres, K and values of the error indicators and condition number for different scaling parameter and $T = 26$. Top table $\lambda = 1$, table in the middle $\lambda = 2$, bottom table $\lambda = 3$. The results in the upper section of each table are obtained using the standard objective function and those in the lower section using the relative objective function. In each section of the tables, results are reported for the standard method (1Sig), for runs in which σ can vary with direction but not with centre (1 × CV), runs in which σ can vary both with direction and centre (Diag), and runs that employ the full covariance matrix (Full). For the standard (1Sig) and 1 × CV runs, the values of the non-zero elements of the Σ matrix are also given.

	1Sig	1 × CV	Diag	Full
$\lambda = 1$, $d = 0.3$, $K = 38$				
$R \times 10^{-2}$	21	18.5	9.0	2.8
e_1	1.7×10^{-1}	1.7×10^{-1}	1.6×10^{-1}	1.2×10^{-1}
$\kappa(B)$	1.8×10^{2}	2.7×10^{2}	1.7×10^{2}	2.3×10^{2}
(σ_1,σ_2)	(0.39, 0.39)	(0.45, 0.39)	"	"
$E_r \times 10^{-2}$	6.3	5.5	1.2	1.0
e_1	7.0×10^{-1}	6.4×10^{-1}	8.3×10^{-2}	1.2×10^{-1}
$\kappa(B)$	1.1×10^{4}	7.5×10^{3}	2.2×10^{4}	5.9×10^{3}
(σ_1,σ_2)	(0.46, 0.46)	(0.51, 0.42)	"	"
$\lambda = 2$, $d = 0.15$, $K = 55$				
$R \times 10^{-2}$	12.7	3.1	3.0	1.8
e_1	1.0×10^{-1}	4.1×10^{-2}	9.2×10^{-2}	6.3×10^{-2}
$\kappa(B)$	6.8×10^{7}	5.0×10^{6}	2.1×10^{7}	8.1×10^{6}
(σ_1,σ_2)	(0.48, 0.48)	(0.65, 0.23)	"	"
$E_r \times 10^{-2}$	3.7	1.1	0.6	0.5
e_1	3.9×10^{-1}	9.5×10^{-2}	8.5×10^{-2}	1.1×10^{-1}
$\kappa(B)$	2.0×10^{7}	4.00×10^{8}	1.0×10^{5}	1.2×10^{5}
(σ_1,σ_2)	(0.40, 0.40)	(0.70, 0.24)	"	"
$\lambda = 3$, $d = 0.09$, $K = 92$				
$R \times 10^{-2}$	10.1	0.6	0.17	0.16
e_1	2.2×10^{-1}	1.6×10^{-2}	1.8×10^{-2}	1.7×10^{-2}
$\kappa(B)$	2.7×10^{7}	8.4×10^{7}	1.0×10^{7}	1.1×10^{7}
(σ_1,σ_2)	(0.25, 0.25)	(0.42, 0.13)	"	"
$E_r \times 10^{-2}$	3.0	0.2	0.09	0.08
e_1	2.4×10^{-1}	1.4×10^{-2}	1.4×10^{-2}	1.3×10^{-2}
$\kappa(B)$	2.4×10^{8}	2.6×10^{8}	8.9×10^{7}	1.7×10^{8}
(σ_1,σ_2)	(0.21, 0.21)	(0.35, 0.11)	"	"

landscape, calculating free-energy activation barriers to diffusion for different processes suggested in the literature [22–24] and comparing the calculated barrier to the the experimental value, $\Delta F_{\text{exp}} = 0.126\,\text{eV}$. We identified a process compatible with experiments: the diffusion of a hydrogen atom from an AlH_6 molecular group in the crystal to the aluminium site (an AlH_5 group) hosting the vacancy. The collective variable chosen to describe this diffusion process was the coordination number [25] of the donor and acceptor Al with respect to the hydrogens (As explained more in detail in the original paper, the coordination number is defined as a smoothed Heaviside function that counts atoms that fall within a certain distance from a reference atom. Due to the smoothing, the coordination number can assume non-integer values, see results below). Preliminary calculations showed it is sufficient to consider hops occurring among pairs of alumina, neglecting correlated motions of other atoms in the crystal. We then concentrated on a representative pair of Al atoms, with coordination numbers C_1 and C_2. In the following, we employ the set of centres used in [16] to repeat the reconstruction of the free-energy landscape in these collective variables with the multivariate Gaussian basis, both for the standard and the relative objective functions. The upper part of Table 4 reports the results of the single sigma, 1 × CV, Diag and Full runs for increasing number of centres and standard objective function. The lower part of the table summarises the results of the single sigma, 1 × CV, Diag and Full runs for the same centres but using the relative objective function. In addition to the value of the appropriate objective function and the condition number, the tables present the results obtained for the free-energy barrier. As in [16], the barrier is found to be asymmetric. This is a consequence of an asymmetry, due to the structure of the crystal lattice, in the local environment of the vacancy when it resides on the different alumina. In the table, ΔF_1 corresponds to the difference of the free energy calculated at the first minimum, $C_1 \approx (5.7, 4.9)$ (see for example the upper panel of Figure 6) and at the saddle point, $C_s \approx (5.1, 4.9)$; ΔF_2 is the difference of the free energy computed at the second minimum, $C_2 \approx (4.9, 5.7)$, and at the saddle point. C_1 corresponds to microscopic configurations in which Al_1 is hexa-coordinated and Al_2 hosts the vacancy, while at C_2

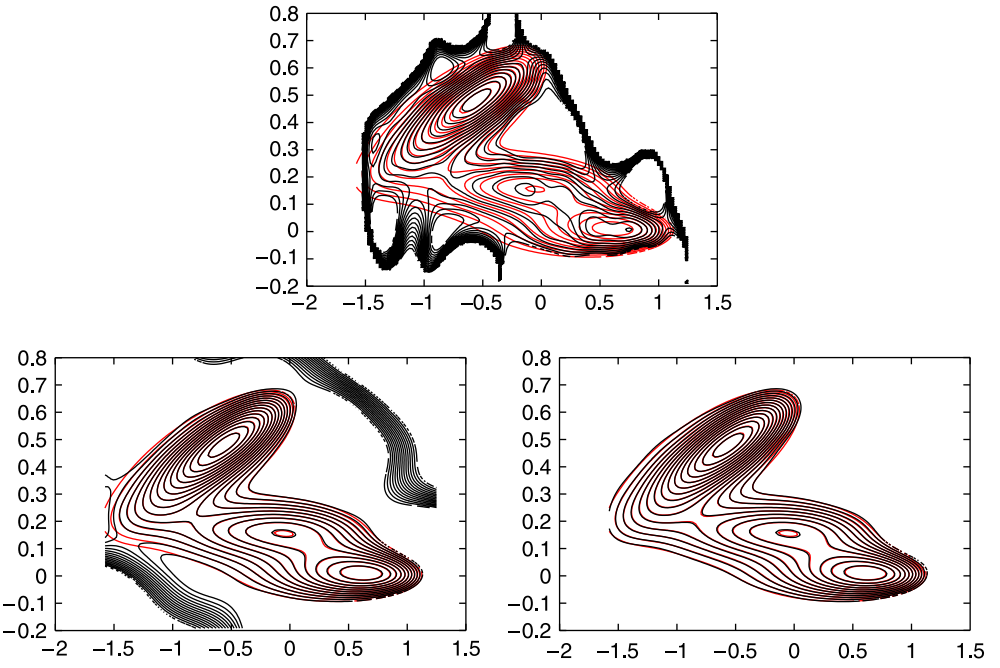

Figure 5. Scaled Müller potential ($\lambda = 3$): Contour lines of the potential from 0 to 140. The red curves are the exact contour lines, the black curves have been reconstructed using the standard single sweep method (upper panel) and 1 × CV runs (lower panel). In the bottom panel, the plot on the left shows the reconstruction with the standard objective function, the plot on the right the reconstruction with the relative objective function. In all figures, the potential was reconstructed using the same 92 centres ($d = 0.09$) deposed along a Langevin trajectory with $T = 26$.

aluminium Al_1 is defective. The values given above for the locations of both the minima and of the saddle point are averaged over the different reconstructions (the values were quite stable in the different reconstructions). Table 4 shows a considerable reduction of the residual when the flexibility of the radial basis is increased. The convergence of the free-energy barriers with increasing number of centres is quite fast both for the standard and the relative objective functions and the values obtained with different methods are always within 0.03 eV. This value ($\approx k_B T$ in the process) is of the order of the typical thermal energy of the system and lower than the accuracy of a DFT calculation, so all our results lead to the same qualitative conclusions on the main features of the activated event. The variations of the standard method, however, introduce some improvements in the reconstruction. Let us focus on the 1 × CV runs that, in the examples considered so far, offer the best compromise among improvements in the reconstruction and added numerical cost of the calculation. Figure 6 shows contour lines of the free energy obtained for 37 (black curves) and 55 (red curves) centres. The upper panel is the result of the standard single sweep reconstruction, while in the lower panel the figures are obtained from 1 × CV calculations performed with the standard (right) and relative (left) objective functions, respectively. The reconstruction that employs the relative objective function shows a better trend to convergence in all relevant regions of the landscape. In particular, both the rise of the free energy from $C_2 \approx (4.9, 5.7)$ to the saddle point and the region around the saddle converge faster and more regularly in this reconstruction. This regularity reflects a more accurate reconstruction of the gradient of the free energy at a set of important centres, some of which are shown in Figure 6. In the figure, the mean force calculated via Equation (6) (green arrows) is compared to that obtained using the gradient of the landscape reconstructed with 37 centres (blue arrows) when the standard (figure on the right) and relative (figure on the left) objective functions are used. The relative objective function consistently provides a more precise estimate of the direction and magnitude of gradients of smaller modulus. These gradients are in the regions where the contour lines obtained with the standard objective function and 37 centres show more relevant differences with those obtained with a larger set of centres. As for the Müller potential, the accurate estimate of the contribution of small gradients proves more important than the accuracy of the reconstruction at points of a large gradient. These are captured more accurately by the standard objective function (see gradient at (4.6,4.8) in the figure), but this fact does not seem to improve the global reconstruction. Note also that the contour lines obtained with the relative objective function and 37 centres are parallel to the lines obtained with the larger set of centres

Table 4. Free-energy barriers for non-local diffusion in sodium alanates for increasing number of centres K. In addition to the values of the condition number κ, the table reports the activation barriers ΔF_1 and ΔF_2 (see text). The objective function used to obtain the results in the upper table $E(a,\Sigma)$, while $E_r(a,\Sigma)$ was employed in the bottom table. Results are reported for the standard method (1Sig), for runs in which σ can vary with direction but not with centre (1 × CV), runs in which σ can vary both with direction and centre (Diag) and runs that employ the full covariance matrix (Full).

	1Sig	1 × CV	Diag	Full
$K = 25$				
$R \times 10^{-2}$	24.0	21.0	4.7	4.0
ΔF_1	0.14	0.12	0.14	0.12
ΔF_2	0.26	0.26	0.25	0.26
$\kappa(B)$	1.1×10^3	3.6×10^2	1.3×10^3	8.1×10^2
$K = 37$				
$R \times 10^{-2}$	19.0	18.4	6.8	4.4
ΔF_1	0.13	0.13	0.14	0.15
ΔF_2	0.24	0.24	0.24	0.24
$\kappa(B)$	8.7×10^2	1.4×10^3	5.1×10^3	6.1×10^3
$K = 55$				
$R \times 10^{-2}$	23.0	18.6	13.4	13.0
ΔF_1	0.13	0.15	0.15	0.15
ΔF_2	0.27	0.27	0.28	0.28
$\kappa(B)$	1.2×10^5	9.8×10^3	6.4×10^4	7.3×10^4
$K = 25$				
$E_r/K \times 10^{-2}$	7.6	6.7	1.1	0.6
ΔF_1	0.15	0.12	0.13	0.14
ΔF_2	0.26	0.25	0.24	0.24
$\kappa(B)$	2.7×10^4	1.2×10^4	1.1×10^4	1.6×10^4
$K = 37$				
$E_r/K \times 10^{-2}$	4.9	4.9	2.0	1.7
ΔF_1	0.13	0.13	0.15	0.15
ΔF_2	0.23	0.24	0.24	0.24
$\kappa(B)$	2.2×10^3	2.6×10^3	4.2×10^3	4.3×10^3
$K = 55$				
$E_r/K \times 10^{-2}$	3.9	3.0	2.4	2.0
ΔF_1	0.14	0.15	0.14	0.14
ΔF_2	0.25	0.25	0.26	0.26
$\kappa(B)$	5.5×10^5	3.7×10^5	4.0×10^5	1.4×10^5

in the basins around the two minima and that, while the area around the saddle point is less accurate, the location of the saddle is also well captured. This suggests that the new objective function allows also for calculating a reasonably accurate minimum free-energy path, and therefore characterising the mechanism of the activated event with a very small number of centres and of evaluations of the mean force. This evaluation can be quite expensive when *ab initio* MD must be used, so being able to reduce the number of centres can have important practical consequences.

5. Conclusions

Two modifications of the single sweep method for reconstructing free-energy landscapes were presented and tested both on a standard model problem and on a physically motivated example. First, the Gaussian radial basis with a single variance used previously in the approach was generalised to include a different covariance matrix for the basis element placed at each centre. Different forms of the covariance matrix were considered to study the effect of the increasing flexibility of the basis set on the quality of the reconstruction. Second, a new objective function tailored to improve the accuracy of the reconstructed free-energy profile in the proximity of stationary points was suggested. A simulated annealing procedure to efficiently minimise the objective function in the presence of the multivariate radial basis set was also introduced. The numerical tests performed in this work show that the generalisation of the Gaussian form can lead to a relevant reduction of the objective function, although establishing in general a stringent correlation among this reduction and an increased accuracy of the reconstruction is non-trivial. On the other hand, the calculations consistently show an improvement of the method for

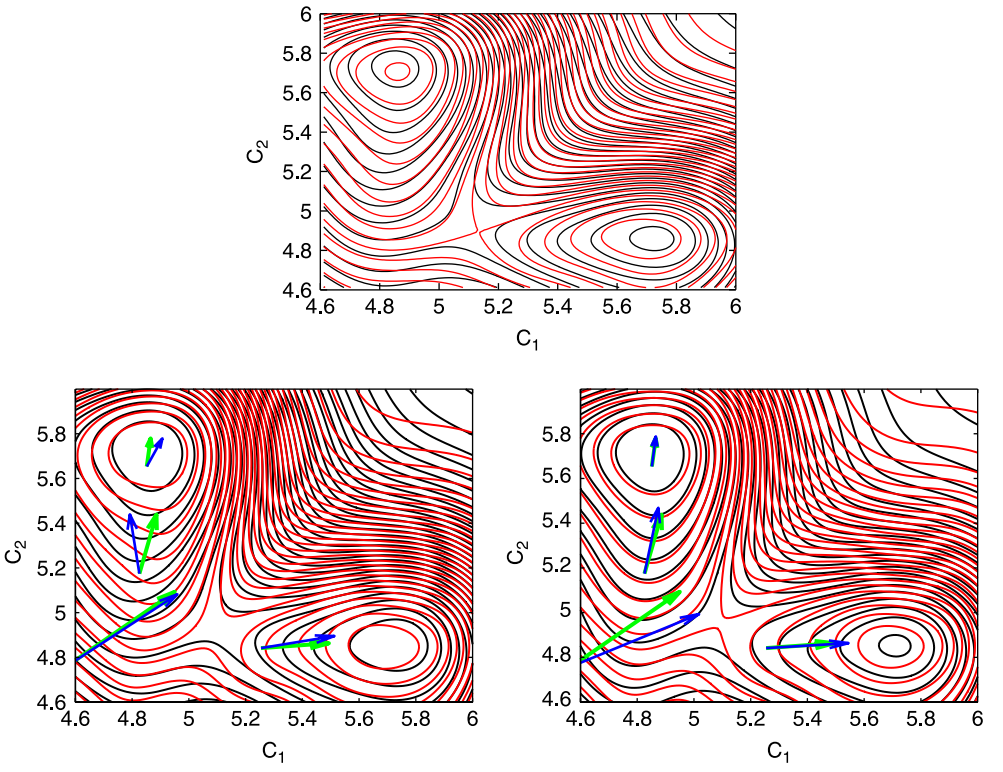

Figure 6. Non-local H diffusion in sodium alanates: Comparison of the contour lines of the free energy reconstructed with 37 (black lines) and 55 (red lines) centres. The upper panel shows the profile reconstructed with the standard single sweep method, while the runs in the lower panel were performed using the 1 × CV version of single sweep for standard (left plot) and relative (right plot) objective function, respectively. The green arrows in the bottom panel are the exact gradients of the free energy computed at a representative subset of centres. The blue arrows are the gradients computed at the same centres from the reconstruction of the free energy based on the standard (left) and relative (right) objective functions. The relative objective function consistently provides a more precise estimate of the direction and magnitude of the gradients of smaller modulus, both close to stationary points and along the steepest descent path.

smaller sets of centres when the relative objective function is used. Our results suggest that the best compromise among accuracy and numerical efficiency is provided by the use of the relative objective function combined with the 1 × CV version of the covariance matrix (i.e. a diagonal form in which the variance is allowed to vary with the component of the collective variable, but not with the centre).

Acknowledgements

This work is dedicated to the memory of Dr J.A. Mejías. The authors wish to thank E. Vanden-Eijnden for many interesting discussions and for careful reading of the manuscript. Funding by a grant of the Ministero dell'Ambiente e della Tutela del Territorio e del Mare is acknowledged.

References

[1] S. Kumar, D. Bouzida, R.H. Swendsen, P.A. Kollman, and J. Rosenberg, *The weighted histogram analysis method for free-energy calculations on biomolecules. I. The method*, J. Comp. Chem. 13 (1992), pp. 1011–1021.

[2] G.M. Torrie and P. Valleau, *Monte Carlo free energy estimates using non-Boltzmann sampling*, Chem. Phys. Lett. 28 (1974), pp. 578–581.

[3] C. Bartles and M. Karplus, *Multidimensional adaptive umbrella sampling: applications to main chain and side chain peptide conformations*, J. Comp. Chem. 18 (1997), pp. 1450–1462.

[4] J.G. Kirkwood, *Statistical mechanics of fluid mixtures*, J. Chem. Phys. 3 (1935), pp. 300–313.

[5] A. Laio and M. Parrinello, *Escaping free energy minima*, Proc. Natl Acad. Sci. USA 99 (2002), pp. 12562–12566.

[6] M. Iannuzzi, A. Laio, and M. Parrinello, *Efficient exploration of reactive potential energy surfaces using Car-Parrinello molecular dynamics*, Phys. Rev. Lett. 90 (2003), 238302.

[7] L. Maragliano and E. Vanden-Eijnden, *Single-sweep methods for free energy calculations*, J. Chem. Phys. 128 (2008), 184110.

[8] L. Maragliano and E. Vanden-Eijnden, *A temperature accelerated method for sampling free energy and determining reaction pathways in rare events simulations*, Chem. Phys. Lett. 426 (2006), pp. 168–175.

[9] J. VandeVondele and U. Rothlisberger, *Canonical adiabatic free energy sampling (cafes): a novel method for the exploration of free energy surfaces*, J. Phys. Chem. B 106 (2002), pp. 203–208.

[10] L. Rosso, P. Minary, Z. Zhu, and M.E. Tuckerman, *On the use of the adiabatic molecular dynamics technique in the calculation of free energy profiles*, J. Chem. Phys. 116 (2002), pp. 4389–4402.

[11] L. Rosso, J.B. Abrams, and M.E. Tuckerman, *Mapping the backbone dihedral free-energy surfaces in small peptides in solution using adiabatic free-energy dynamics*, J. Phys. Chem. B 109 (2005), pp. 4162–4167.

[12] J.B. Abrams and M.E. Tuckerman, *Efficient and direct generation of multidimensional free energy surfaces via adiabatic*

dynamics without coordinate transformations, J. Phys. Chem. B 112 (2008), pp. 15742–15757.
[13] R. Schaback, *Error estimates and condition numbers for radial basis function interpolation*, Adv. Comp. Math. 3(1) (1995), pp. 251–264.
[14] M.D. Buhmann, *Radial basis functions: the state-of-the-art and new results*, Acta Numer. (2000), pp. 1–38.
[15] K. Müller, *Reaction paths on multidimensional energy hypersurfaces*, Angew. Chem. 92 (1980), pp. 1–13.
[16] M. Monteferrante, S. Bonella, S. Meloni, E. Vanden-Eijnden, and G. Ciccotti, *Calculations of free energy barriers for local mechanisms of hydrogen diffusion in alanates*, Scient. Model. Simul. 15 (2008), pp. 187–206.
[17] G.H. Golub and C.F. Van Loan, *Matrix Computations*, Johns Hopkins University Press, Baltimore and London, 1996.
[18] P. Brémaud, *Markov Chains, Gibbs Fields, Montecarlo Simulations, and Queues*, Springer, New York, 1999.
[19] L. Maragliano, A. Fischer, E. Vanden-Eijnden, and G. Ciccotti, *String method in collective variables: minimum free energy paths and isocommittor surfaces*, J. Chem. Phys. 125 (2006), 024106.
[20] E. Vanden-Eijnden and G. Ciccotti, *Second-order integrators for langevin equations with holonomic constraints*, Chem. Phys. Lett. 429 (2006), pp. 310–316.
[21] B. Bogdanovi, and M. Schwickardi, *Ti-doped alkali metal aluminium hydrides as potential novel reversible hydrogen storage materials*, Journal of Alloys and Compounds 1 (1997), pp. 253–254.
[22] O. Palumbo, R. Cantelli, A. Paolone, C.M. Jensen, and S.S. Srinivasan, *Point defect dynamics and evolution of chemical reactions in alanates by anelastic spectroscopy*, J. Phys. Chem. B 109 (2005), pp. 1168–1173.
[23] O. Palumbo, A. Paolone, R. Cantelli, C.M. Jensen, and M. Sulic, *Fast H-vacancy dynamics during alanate decomposition by anelastic spectroscopy. Proposition of a model for ti-enhanced hydrogen transport*, J. Phys. Chem. B 110 (2006), pp. 9105–9111.
[24] J. Voss, Q. Shi, H.S. Jacobsen, M. Zamponi, K. Lefmann, and T. Vegge, *Hydrogen dynamics in Na_3AlH_6: a combined density functional theory and quasielastic neutron scattering study*, J. Phys. Chem. B 111 (2007), pp. 3886–3892.
[25] M. Sprik, *Computation of the pK of liquid water using coordination constraints*, Phys. Chem. 258 (2000), pp. 139–150.

Appendix A: Summary of the optimisation algorithm

The optimisation of the coefficients $\{a_k\}$ and of the elements in the covariance matrix $\{\Sigma\}$ to minimise either the standard objective function, Equation (8), or the relative objective function, Equation (19), can be performed as follows: (1) select a value for the matrix elements $(\Sigma_k)_{\alpha,\beta}$; (2) for this choice of $\{\Sigma\}$ solve the appropriate linear system of Equations (Equation (17) for the standard objective function, or Equation (20) for the relative objective function) and compute the corresponding residual; (3) iterate the first two steps until convergence to the minimum of the objective function is reached. The solution of the linear system can be obtained using, for example, standard lapack (www.netlib.org/lapack/) libraries. For a high dimensional Σ matrix, and large sets of centres, the non-trivial step in the minimisation of the objective function is performing a search in the space of the $\{\sigma_{k,\alpha}, \rho_{k,\alpha,\beta}\}$ that will rapidly converge to the minimum of the objective function. An efficient solution to this problem is offered by simulated annealing [18]. Let us consider first the case of the standard objective function (the calculation for the relative objective function requires only one modification described at the end of this appendix). In this case, we choose to minimise the relative residual, $R(a^*, \{\Sigma\})$ defined in Equation (14) ($R(a^*, \{\Sigma\})$ has the same minimum as the standard objective function). In the annealing, a Metropolis Monte Carlo exploration of the $\{\sigma_{k,\alpha}, \rho_{k,\alpha,\beta}\}$ is performed. The generation of the trial moves in the Monte Carlo requires some care to ensure that Σ remains positive definite at all steps of the annealing. We enforced this property by using moves that would conserve it by construction. The run uses as initial condition a diagonal covariance matrix which can easily be constructed to be positive definite. At each Monte Carlo step a 'diagonal' (i.e. a move on $\sigma_{k,\alpha}$) or an 'off-diagonal' (i.e. a move on $\rho_{k,\alpha,\beta}$) move is selected. This is done by extracting randomly a pair of indexes that identify a matrix element $\{\Sigma\}$. If a diagonal element, $\sigma^2_{k,\alpha}$, is selected for the move, then it is changed by adding to it an appropriate random displacement, with the requirement that the new diagonal element be non-negative. All off-diagonal elements of the form $\sigma_{k,\alpha}\sigma_{k,\beta\neq\alpha}$ are updated with the new value of $\sigma_{k,\alpha} > 0$. Similarly, a Monte Carlo move for the correlation coefficient $\rho_{k,\alpha,\beta}$ is performed by resampling its value uniformly between minus one and one and then updating $\rho_{k,\alpha\beta}\sigma_{k,\alpha}\sigma_{k,\beta}$ and the corresponding symmetric matrix element $\rho_{k,\beta,\alpha}\sigma_{k,\beta}\sigma_{k,\alpha}$. Either move preserves by construction the properties of the elements of a covariance matrix and the resulting trial matrix is therefore guaranteed to be positive definite and to produce a multivariate Gaussian when used in the definition of our basis functions. The trial matrix, Σ', is then inverted – an operation that does not change the positive definite nature of a matrix since it preserves the sign of the eigenvalues – and used to find the new a^* and to compute $R(a^*(\Sigma'), \Sigma e)$. This function is used in the Metropolis test: the new matrix is accepted or rejected based on the acceptance probability

$$\mathrm{A} = \min\left(1, \mathrm{e}^{-\beta_f[R(a^*(\Sigma'),\Sigma')-R(a^*(\Sigma),\Sigma)]}\right). \tag{A1}$$

The parameter β_f in this equation is analogous to the inverse temperature. This parameter is set initially to a small enough value to allow for a relatively easy exploration of the R landscape even in the presence of local minima and significant barriers. As the exploration of the $\{\Sigma\}$ combinations proceeds, record is kept of the lowest value obtained for the relative residue. After an appropriate number of moves the Monte Carlo run is reinitialised: β_f is increased and new trial moves are generated starting from the Σ configuration corresponding to the lowest value of the relative residue at the previous temperature. The procedure is repeated according to a fixed 'cooling' schedule that ensures both a sufficient exploration of the $\{\sigma_{k,\alpha}, \rho_{k,\alpha,\beta}\}$ states at each temperature, and that the simulation is efficiently quenched towards a minimum of R. Although there is no guarantee that the simulated annealing will reach the global minimum of the target function, it should converge towards a good solution of the optimisation problem. The danger of getting trapped in local minima of the target function can be reduced by checking the stability of the optimal $\{\Sigma\}$ configuration with respect to the choice of the initial configuration and of the cooling schedule enforced in the simulation.

The minimisation of the relative objective function proceeds in complete analogy with the one just described, with the only difference that the trial moves are judged based on the function

$$P_r(\{\Sigma\}) \propto \mathrm{e}^{-\beta_f((E_r(a^*,\Sigma))/K)}, \tag{A2}$$

where K is the number of centres and the relative objective function $E_r(a^*, \Sigma)$ is defined as in Equation (19). The applications that we show in this paper allow, in some cases, for simplifications in the procedure. For example, when the number of collective variables is equal to two, the covariance matrix can be inverted analytically and the moves simplified. All calculations were however performed using the algorithm just described to test its performance in view of more general situations.